separations

MDPI

Article

Bismuth Oxychloride@Graphene Oxide/Polyimide Composite Nanofiltration Membranes with Excellent Self-Cleaning Performance

Runlin Han [1,†], Faxiang Feng [1,†], Zanming Zhu [1,†], Jiale Li [1], Yiting Kou [1], Chaowei Yan [1] and Hongbo Gu [2,*]

[1] Key Laboratory of Jiangxi Province for Special Optoelectronic Artificial Crystal Materials, School of Chemistry and Chemical Engineering, Jinggangshan University, Ji'an 343009, China; hanrunlin@jgsu.edu.cn (R.H.)
[2] Key Laboratory of Chemical Assessment and Sustainability, School of Chemical Science and Engineering, Tongji University, Shanghai 200092, China
* Correspondence: hongbogu2014@tongji.edu.cn
† These authors contributed equally to this work.

Abstract

Organic pollution poses a serious threat to global water safety, while traditional treatment technologies suffer from low efficiency, high costs, and secondary pollution issues. This study successfully develops a highly efficient separation and photocatalytic degradation composite bismuth oxychloride@graphene oxide/polyimide (BiOCl@GO/PI) membrane by loading GO and BiOCl photocatalysts onto PI supporting membrane. The results show that this composite membrane achieves a rejection of 99.8% for methylene blue (MB) and 87.6% for tetracycline hydrochloride (TC). Under UV irradiation, the membrane exhibits a retention rate decline of only 6.8% after five cycles, with water flux stably maintaining at 605 L m^{-2} h^{-1} bar^{-1}. Compared to dark conditions, it demonstrates remarkable flux recovery. This is attributed to the membrane's excellent photocatalytic degradation activity under UV irradiation. After five degradation cycles, the degradation efficiency is decreased from 97.5 to 88.3%. Studies on radical scavengers indicate that UV irradiation generates free radicals, thereby conferring excellent catalytic activity to the membrane. Its unique synergistic effect between separation and photocatalysis endows it with outstanding self-cleaning performance. This research provides an innovative integrated solution for antibiotic pollution control, demonstrating significant potential for environmental applications.

Keywords: antibiotic treatment; membrane separation; BiOCl@GO/PI composite membrane; photocatalytic degradation; self-cleaning

Check for updates

Received: 5 December 2025
Revised: 11 January 2026
Accepted: 13 January 2026
Published: 16 January 2026

Copyright: © 2026 by the authors. Licensee MDPI, Basel, Switzerland. This article is an open access article distributed under the terms and conditions of the Creative Commons Attribution (CC BY) license.

1. Introduction

With the rapid advancement of industrialization, pollutants such as dyes and antibiotics have been discharged in large quantities into water bodies [1–3]. These contaminants not only directly impact the ecological health of water bodies and destroy the habitats of aquatic organisms, but also pose potential threats to human health [4,5]. Numerous novel water treatment technologies, including adsorption, membrane separation, electrocatalysis and photocatalysis, have been applied to the treatment of organic pollutants such as antibiotics [6–8]. Amongst the technologies, membrane separation technology is widely adopted due to its many advantages, like energy efficiency, environmental friendliness, cost-effectiveness, compact footprint, and ease of integration with other processes [9,10]. Unfortunately, due to the complexity of wastewater, many membranes exhibit

low separation selectivity and suffer from severe fouling during operation, leading to rapid deterioration in membrane performance and limiting their widespread application [11,12].

Photocatalytic membranes consist of nanocatalysts embedded and immobilized within a polymer or ceramic membrane substrate, where the activity of nanocatalysts is achieved through direct light irradiation of the membrane surface [13]. The combination of membrane separation technology and photocatalysis process could produce synergistic effects. On one hand, the photocatalyst could effectively degrade pollutants on the membrane surface, significantly mitigating fouling issues. On the other hand, the immobilized photocatalyst could ensure thorough contact with pollutants for efficient degradation [14–16]. Yu et al. [14] prepared a novel photocatalytic polysulfone ultrafiltration (UF) membrane by adding mesoporous graphitic carbon nitride/titanium dioxide nanocomposite with the phase inversion method. This membrane was able to degrade the antibiotic sulfamethoxazole efficiently when exposed to the sunlight. Zhang et al. [15] loaded TiO_2 nanofibers onto the surface of hollow fiber ceramic membranes by using an immersion coating method, which achieved a removal rate up to 90% for humic acid and demonstrated an excellent anti-fouling capability. However, conventional photocatalytic membrane catalysts are often embedded within the membrane matrix, leading to severe encapsulation of the catalyst. Alternatively, the preparation process for catalytic membranes is highly complex, limiting their widespread application. Therefore, it is necessary to develop novel composite catalytic membranes that simplify the preparation process while maintaining their high catalytic activity [17].

Recently, graphene oxide (GO)-laminated membranes have been extensively studied since they exhibit outstanding molecular separation performance [18,19]. Ruiz–Torres et al. [20] developed oxidation-controlled nanoporous graphene laminate membranes by using graphite intercalation chemistry, creating nanopores (1–4.5 nm) with controlled oxidation to prevent excessive interlayer spacing. In forward osmosis desalination, the membranes could effectively remove >98–99% of typical seawater ions and maintain high performance under acidic conditions, chlorine exposure, and prolonged use (30 days). Ma et al. [21] developed a bimetallic MOF (Ti, Zr) composite membrane (GO/UIO@MIL) by using an MOF-on-MOF growth strategy. The hydrophilic MOF with micro/nano-rough architecture provided the membrane with excellent anti-fouling properties, which exhibited a high permeation flux (>2010 L m^{-2} h^{-1} bar^{-1}) and >99.4% separation efficiency for oil-in-water emulsions. Joseph et al. [22] investigated the removal of carbamazepine (CBZ) by reduced graphene oxide (rGO) as both an adsorbent and a carrier for TiO_2 photocatalyst, which resulted in 39.8% of CBZ removal. It demonstrated the potential application of rGO for removing persistent pharmaceuticals in advanced water treatment technologies. Hence, high-performance composite membranes for antibiotic wastewater treatment might be obtained by designing or modifying GO membranes [23,24].

Bismuth oxychloride (BiOCl) is an excellent photocatalyst material, exhibiting high catalytic activity and chemical stability, with its morphology easily tuned. It demonstrated an outstanding photocatalytic activity in dye and antibiotic degradation [7,25,26]. BiOCl photocatalysts are typically nanomaterials used in suspensions, requiring subsequent filtration and recovery after use, which increases wastewater treatment costs and process complexity [27]. Due to the poor affinity between inorganic nanomaterials and polymer matrices, it is difficult to maintain stable presence on membrane surfaces [28]. Therefore, a photocatalytic membrane based on BiOCl with both excellent photocatalytic and separation properties has not been reported yet.

Based on the aforementioned, this study ingeniously introduces $BiCl_3$ into the GO membrane solution. Through vacuum filtration self-assembly on a polyimide (PI) support membrane, a photocatalytic BiOCl@GO/PI composite membrane with outstanding photo-

catalytic performance and separation selectivity is prepared. The preparation process of the membrane fully leverages the hydrolysis of $BiCl_3$ to form BiOCl. During the formation of the membrane, the polymerization reaction of dopamine hydrochloride (DA·HCl) produces polydopamine (PDA) and enhances the bonding strength between the PI support, GO, and BiOCl, resulting in a highly stable composite membrane. This approach achieves uniform dispersion of the nanocatalyst, avoiding the loss of the catalyst. This approach achieves highly synergistic membrane separation and photocatalytic reactions. Detailed investigations are conducted on the membrane's separation selectivity and anti-fouling performance, while also exploring the catalytic membrane's cycling stability and degradation mechanisms. This research provides a novel solution for the efficient treatment of antibiotic and dye wastewater.

2. Materials and Methods

2.1. Materials

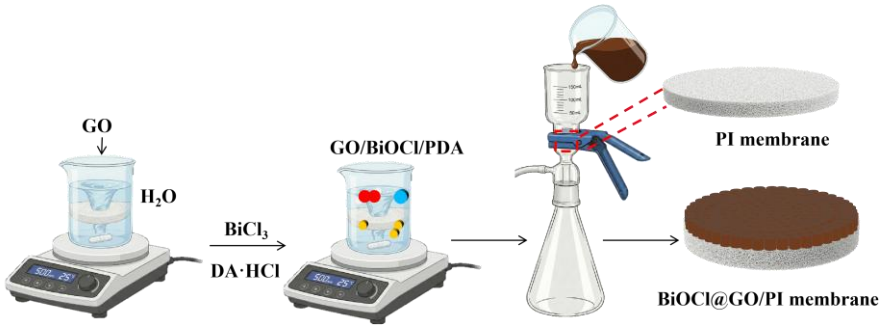
PI (P84, M_w: 25,000) was provided by HP Polymer Inc. (Linz, Austria). Graphene oxide (GO) multilayer nanosheets (Tanfeng Tech Inc., Suzhou, China) were used as the functional layer material. *N*,*N*-dimethylacetamide (DMAc), polyvinylpyrrolidone (PVP, K30), DA·HCl, $BiCl_3$, ciprofloxacin (CIP, $C_{17}H_{18}FN_3O_3$, M_w: 331.34), tetracycline hydrochloride (TC·HCl, $C_{22}H_{25}ClN_2O_8$, M_w: 480.9), Rhodamine B (RhB, $C_{28}H_{31}ClN_2O_3$, M_w: 479.01), methylene blue (MB, $C_{16}H_{18}ClN_3S$, M_w: 319.85), isopropanol (IPA), ethylenediaminetetraacetic acid disodium salt (EDTA-2Na), and p-benzoquinone (PBQ) were all analytical grade and obtained from Aladdin (Shanghai, China) without further purification.

2.2. Preparation of the Composite Membrane

According to our previous work [29], the PI support membrane cast on polyester nonwovens with 14 wt.% of PI and 3 wt.% of PVP in DMAc solution was prepared by the immersion phase inversion method using deionized water as the coagulation bath, which was designated as M0 and selected as the control sample. The experimental procedure for preparing composite materials including M1, M2, and M3 via the filtration method was as follows [30]. M1 was taken as an example. First, 20 mg of GO was dispersed in 50 mL of deionized water and subjected to ultrasonic treatment for 20 min to obtain a uniformly dispersed solution. Subsequently, the system was magnetically stirred under constant temperature at 40 °C. A total of 10 mL of $BiCl_3$ ethanol solution (2 g L^{-1}) was added into the system dropwise at a rate of 1 mL min^{-1} by using a dropping funnel. After that, the ultrasonic treatment was continued at 40 °C for 20 min. Next, a total of 10 mg of DA·HCl was added into the system and maintained ultrasonication at 40 °C for 20 min to achieve the uniform formation of the composite. Under continuous magnetic stirring, 10 mL of $KMnO_4$ solution (2 g L^{-1}) was slowly added at the same rate. Finally, the resulting mixed suspension was vacuum filtered by using a vacuum filtration apparatus to uniformly deposit the product onto the surface of the PI substrate membrane. For M2 membrane, DA·HCl and $BiCl_3$ contents were changed to 20 and 2.5 mg, respectively. For M3 membrane, DA·HCl and $BiCl_3$ contents were both changed to 20 mg. The preparation procedure and membrane composition are shown in Scheme 1 and Table 1.

Table 1. Composition of the membrane solution.

Name	GO (mg)	DA·HCl (mg)	$BiCl_3$ (mg)
M0	0	0	0
M1	20	10	2.5
M2	20	20	2.5
M3	20	20	20



Scheme 1. The preparation procedure of composite membrane.

2.3. Characterizations

Contact angle goniometer (CA100A, Shanghai Innuo Precision, Shanghai, China) was used to test the surface hydrophilicity of the membrane. The membranes were coated with a thin layer of gold to capture the scanning electron microscope (SEM, ZEISS Sigma 300, Oberkochen, Germany) image at an acceleration voltage of 15 KV. Meantime, the energy dispersive spectroscopy (EDS, Oxford Xplore 30, Oxford, UK) was used for elemental content analysis. The elemental composition of the material was analyzed using an X-ray photoelectron spectrometer (XPS, ESCALAB 250Xi, ThermoFisher, MA, USA). An X-ray diffractometer (XRD, Rigaku SmartLab SE, Tokyo, Japan) was applied to analyze the diffraction patterns of membranes with a scanning range from 5 to 60° at a scanning rate of 5° min^{-1}.

2.4. Separation and Photocatalytic Performance Examination of BiOCl@GO/PI Membrane

The membrane flux (F) was characterized by the setup of solvent filter with a dead-end method under a vacuum pump at room temperature, which was calculated by Equation (1).

$$F = \frac{W}{At} \tag{1}$$

where W (L) was the total volume of water or solution permeated during filtration process, A (m^2) was the effective membrane area, and t (h) was the operating time.

The concentrations of salt were determined by conductance meter (DDS-11A, Leici, Shanghai, China) and the concentrations of organic compounds were tested with a UV-vis spectrophotometer (UV-4501S, Tianjin Gangdong Science and Technology Development, Tianjin, China). The membrane rejection (R) was computed by Equation (2):

$$R = 1 - \frac{c_p}{c_f} \tag{2}$$

where c_p (mg L^{-1}) and c_f (mg L^{-1}) were the concentration of the permeate and feed solution, respectively.

The photocatalytic degradation rate (D) of CA/BiOCl membranes with a diameter of 60 mm under UV irradiation in 10 mg L^{-1} of TC (100 mL) was evaluated. A 36 W UV lamp (254 nm) was used as the light source. After the degradation system was left in the dark for 30 min to equilibrate the adsorption, the UV lamp was switched on for irradiation, and the same volume of sample solution (2 mL) was taken out at every half an hour. The absorbance was then measured by using a UV-vis spectrophotometer, and the photocatalytic degradation efficiency of the composite membrane was calculated by Equation (3):

$$D\ (\%) = \frac{C_0 - C_t}{C_0} \tag{3}$$

where C_0 (mg L^{-1}) and C_t (mg L^{-1}) were the initial absorbance and absorbance at time t for TC (or other organics), respectively.

2.5. Photocatalytic Mechanism and Cycle Stability Study of BiOCl@GO/PI Membrane

To detect the specific active species in the photocatalytic process, hydroxyl radical (·OH), superoxide radical ($\cdot O^{2-}$), and hole (h^+) were investigated by adding trapping agents IPA, PBQ, or EDTA-2Na, respectively. The method was similar to the former photocatalytic activity test with the addition of 1 mM of quencher into 200 mL of RhB solution (20 mg L^{-1}) with photocatalytic membrane [31]. The BiOCl@GO/PI composite membrane was added into the solution and exposed to UV light at 254 nm for 6 h. The absorbance before and after treatment was measured by using a UV-vis spectrophotometer, then photocatalytic degradation efficiency was calculated according to Equation (3). By comparing the degradation rate with that of the solution without the scavenger, the radical species involved in the scavenging process and their influence intensity were examined.

To investigate the performance of BiOCl@GO/PI composite membranes in the cyclic photocatalytic degradation of TC, 100 mL of a 0.01 g L^{-1} TC solution was placed in a 250 mL beaker. A 60 mm membrane sample was then introduced into the solution-containing beaker. First, the membrane was placed in a dark, stationary TC solution for 30 min to reach the adsorption equilibrium. After measuring the absorbance, the membrane was exposed to UV light. Absorbance measurements were conducted every 2 h. The 60 mm membrane sample was reused for five times. After each use, the membrane was immersed in 150 mL of anhydrous ethanol for 12 h to clean the membrane.

To investigate the self-cleaning performance of the BiOCl@GO/PI composite membrane, the same membrane was subjected to five consecutive cycles of excess filtration. Each filtration cycle involved filtering 100 mL of a 20 mg L^{-1} RhB solution (200 mL). After filtration, 200 mL of clean water was added and then the membrane was exposed to 254 nm UV irradiation for 3 h before initiating the next cycle.

3. Results and Discussion

3.1. Membrane Characterization

The SEM images of M0 and M1 are shown in Figure 1. It is observed that M0 shows a porous structure with uniform pores about 1 μm; see Figure 1a–c. With the introduction of the GO functional layer, the membrane surface is changed from a loose and smooth structure to a dense and rough one; see Figure 1d–f. It also reveals ultra-thin, highly dense GO nanosheets. Figure 1g–i shows the rough surface of the M3 membrane because of the large content of BiOCl crystals in the membrane surface. As shown in the elemental mapping, Figure 1j–o, C, O, N, Cl, and Bi elements are uniformly distributed in the M1, confirming the successful fabrication of the BiOCl@GO/PI composite membrane. The N element is originated from the PI backbone, and the Bi and Cl elements are derived from the BiOCl nanocrystals. No large nanoparticles are observed on the surface of M1, implying that BiOCl is formed with a very homogeneous distribution by in situ growth of $BiCl_3$ during immersion in water coagulation bath.

The elemental composition of the composite membrane is shown in Table 2. The C content is relatively high (45.97%), primarily originating from the support film and GO. However, the membrane also exhibits elevated levels of Bi (10.53%) and Cl (13.91%), attributed to the formation of substantial amounts of BiOCl crystals intercalated between graphene oxide layers.

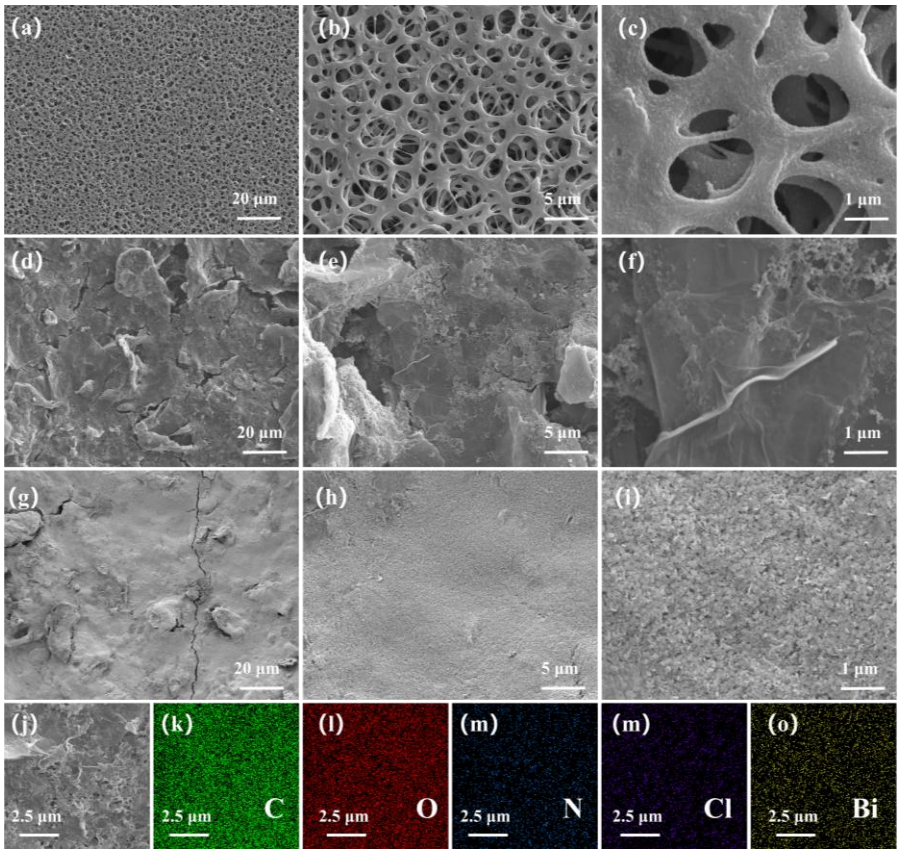


Figure 1. SEM images of membranes at different magnifications (**a**–**c**) M0, (**d**–**f**) M1, and (**g**–**i**) M3; (**j**) EDS zero-loss image and elemental mapping images (**k**–**o**) of C, O, N, Cl, and Bi elements of M1.

Table 2. Element composition of the composite membrane M1.

Element	Atomic %
Bi 4f	10.53
C 1s	45.97
Cl 2p	13.91
N 1s	5.84
O 1s	23.74

The cross-sectional structures of M0 and M1 were also examined by SEM and the results are shown in Figure 2. The cross-section of the support membrane exhibits a high porosity, displaying a typical sponge-like pore structure. It is clearly seen that the layer structure of composite differs markedly from the support layer. In addition, the composite layer structure is relatively dense, with a thickness of approximately 28.5 μm.

The AFM morphologies of the composite membrane M1 with a fixed scan area of 3 μm × 3 μm have been provided. As illustrated in Figure 3, the membrane surface displays an average roughness (Ra) of 5.498 nm, indicating a relatively rough topography. The 3D-view image of the composite membrane reveals peak-like protrusions on the composite membrane surface, which may originate from BiOCl nanocrystals and PDA nanospheres in the GO layer.

Figure 4a shows FTIR spectra of M0 and the composite membranes (M1, M2, and M3). The characteristic absorption peaks at 1778 and 1724 cm^{-1} belong to the stretching vibration of C=O in the backbone of PI. The absorption peak located at 1310 cm^{-1} is assigned to the stretching vibration of C-N of PI. For M1, the characteristic adsorption peaks of PI disappeared because infrared beams cannot penetrate the GO membrane of the functional

layer. The characteristic peak at 1573 cm^{-1} corresponds to the N-H characteristic peak of PDA, and one at 1048 cm^{-1} is assigned to the C-O-C stretching vibration of GO [32]. These results indicate that BiOCl@GO/PI composite membranes with in situ grown BiClO have been successfully prepared [31].

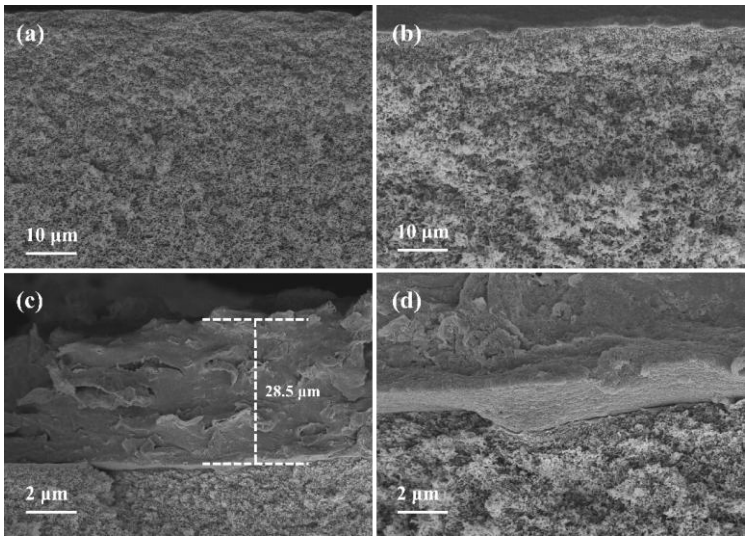


Figure 2. Cross-sectional SEM images of membranes at different magnifications (**a**,**b**) M0 and (**c**,**d**) M1.

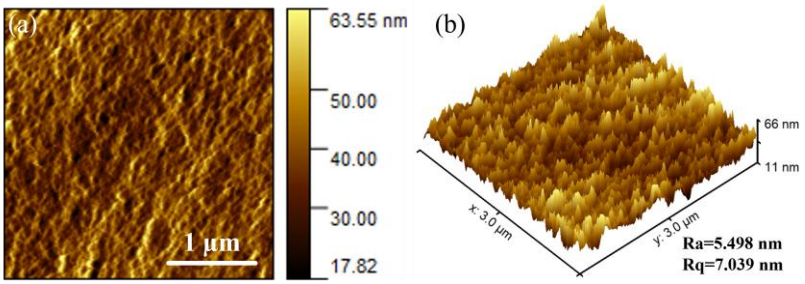


Figure 3. AFM images of composite membrane M1: (**a**) 2D view; (**b**) 3D view.

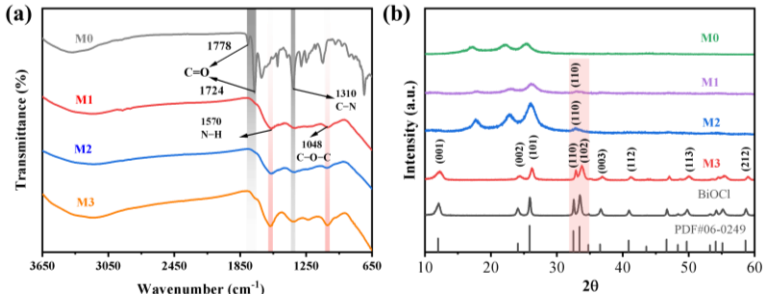


Figure 4. (**a**) FTIR spectra of membranes; (**b**) XRD patterns of BiOCl and membranes.

Figure 4b shows XRD patterns of pure BiOCl, M0, M1, M2, and M3 membranes. The BiOCl sample has several diffraction peaks at $2\theta = 11.99°$, 24.10°, 32.53°, and 46.64° for (001), (002), (110), and (200), respectively, corresponding to the crystallographic planes of BiOCl (PDF#06–0249). These diffraction peaks are also observed in the M3 sample, suggesting a successful synthesis of BiOCl in the membrane. For M1 and M2 samples, peaks for (101) and (110) also appear in the XRD patterns. The relatively high PDA content may be responsible for the weaker intensity of the crystalline peaks. Since PI is a non-crystalline polymer, it has no distinct crystalline peaks.

The composite membrane M1 was also tested by XPS. In Figure 5a, the wide-scan XPS spectrum provides the chemical composition of M1. It is noticed that the functional layer of M1 primarily contains elements such as C, O, N, Cl, Bi elements. Table 1 illustrates the content of various elements. The atomic content ratio of Bi and Cl elements reaches 10.53 and 13.91%, respectively, indicating that a significant amount of BiOCl is successfully incorporated into the functional interlayers of GO. In the high-resolution XPS C 1s spectrum of Figure 5b, there are three peaks at 287.7, 286.2, and 284.8 eV, corresponding to C=O, C-N/C-O, and C-C, respectively. Figure 5c shows the high-resolution XPS O 1s spectrum with three deconvoluted binding energy peaks at 532.45, 530.85, and 529.98 eV, respectively. These peaks are from C-O, C=O, and Bi-O groups of GO, PDA, and BiOCl. Figure 5d provides the high-resolution XPS N 1s spectrum, depicting two fitted peaks centered at 401.59 and 399.78 eV that are originated from PDA and attributed to pyrrolic N and pyridinc N, respectively. Figure 5e exhibits two binding energy peaks centered at 199.5 and 197.2 eV that can be assigned to the Cl $2p_{3/2}$ and Cl $2p_{1/2}$, respectively. Figure 5f displays two binding energy peaks at 164.5 and 159.2 eV, which are assigned to Bi $4f_{7/2}$ and Bi $4f_{5/2}$, respectively [33]. These results confirm the presence of BiOCl in the composite membrane.

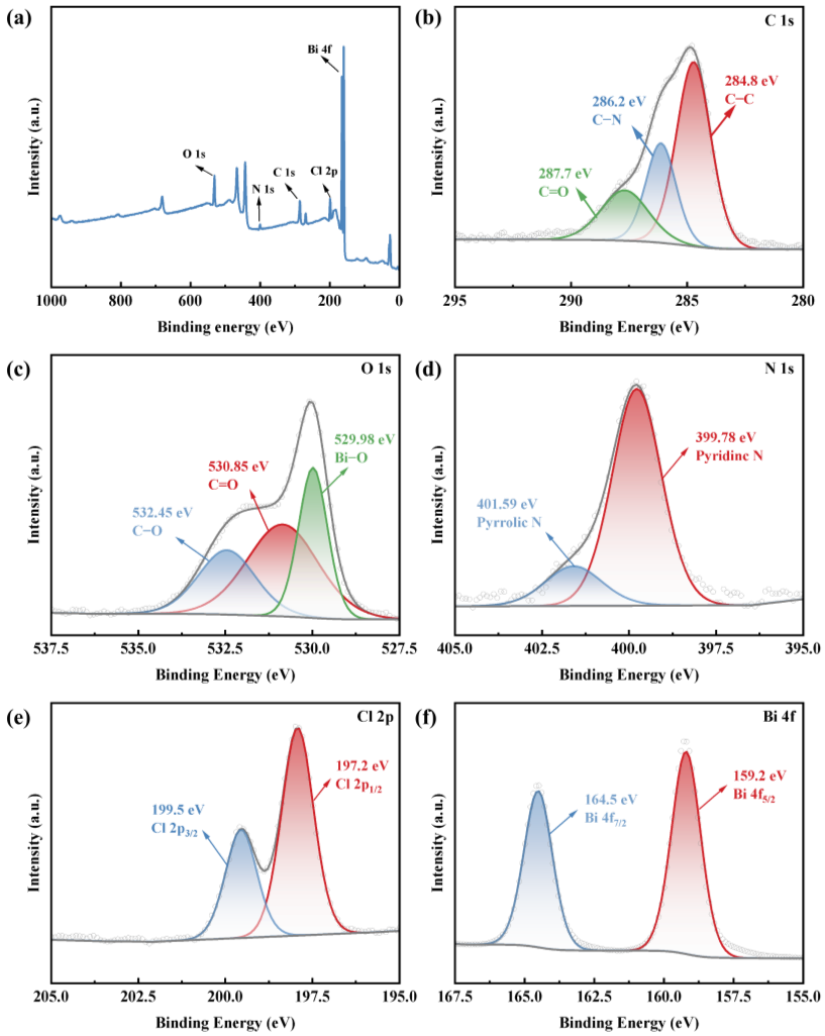


Figure 5. (**a**) Wide-scan XPS spectrum of M1; high-resolution XPS spectra of (**b**) C 1s, (**c**) O 1s, (**d**) N 1s, (**e**) Cl 2p, and (**f**) Bi 4f of M1.

3.2. Separation Performance of the BiOCl@GO/PI Membrane

The water contact angle and pure water flux of M0–M3 were tested, and the data are shown in Figure 6. The water contact angles of M0, M1, M2, and M3 are found to

be 63.5°, 26.4°, 21.1°, and 11.9°, respectively. These values decrease significantly with the addition of $BiCl_3$ during membrane preparation. This suggests that these composite membranes are much more hydrophilic than the support membrane, primarily due to the presence of hydrophilic GO, BiOCl nanocrystals, and PDA in the functional layer. The M0 exhibits a high pure water flux of 5425 L (m^{-2} h^{-1} bar^{-1}) due to its loose structure, as demonstrated in SEM images. However, upon introducing the functional layer of GO, the dense composite membrane structure results in significant mass transfer resistance, causing the decrease in the membrane flux to 636 L (m^{-2} h^{-1} bar^{-1}). Despite variations in $BiCl_3$ and DA·HCl contents, the membrane flux remains relatively stable, indicating that mass transfer resistance is primarily concentrated on GO nanosheets.

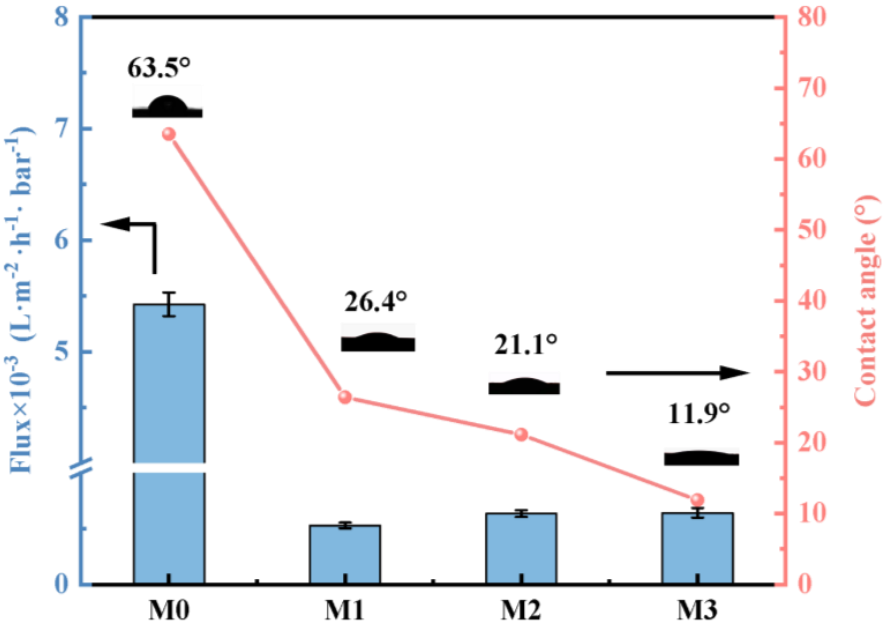


Figure 6. Pure water flux and water contact angle of the membranes. The direction of arrow means the corresponding *y* axis.

The separation selectivity of M0 and composite membranes M1–M3 to inorganic salts, such as NaCl, Na_2SO_4, $MgCl_2$, as well as organics, such as TC, CIP, RhB and MB, was tested, and the results are shown in Figure 7. Due to its large pore size and relatively loose structure, the M0 membrane has a very high permeate flux and low rejection of most solutes, except MB. The high rejection of MB may be due to the strong electrostatic attraction between its positive charge and the negative charge of residual carboxyl groups on the PI backbone. The introduction of the dense functional layer GO causes the rapid decrease in permeate flux. Furthermore, with increasing BiOCl concentrations, the membrane exhibits gradually increasing flux. This may be from an increased formation of BiOCl nanocrystals that are intercalated into GO nanosheets. This intercalation increases the interlayer spacing, enhancing permeate flux. At the same time, the M3 exhibits an improved rejection to inorganic salts, such as NaCl (5.9%), $MgCl_2$ (8.6%), and Na_2SO_4 (16.8%), as well as organics, such as TC (87.6%), CIP (92.5%), MB (99.9%), and RhB (97.1%). Notably, the rejection of different antibiotics by the M3 increases significantly, while the rejections of inorganic salts are lower than 16.8%. Therefore, the composite membrane M3 can be used for desalination of antibiotics with high selectivity [29].

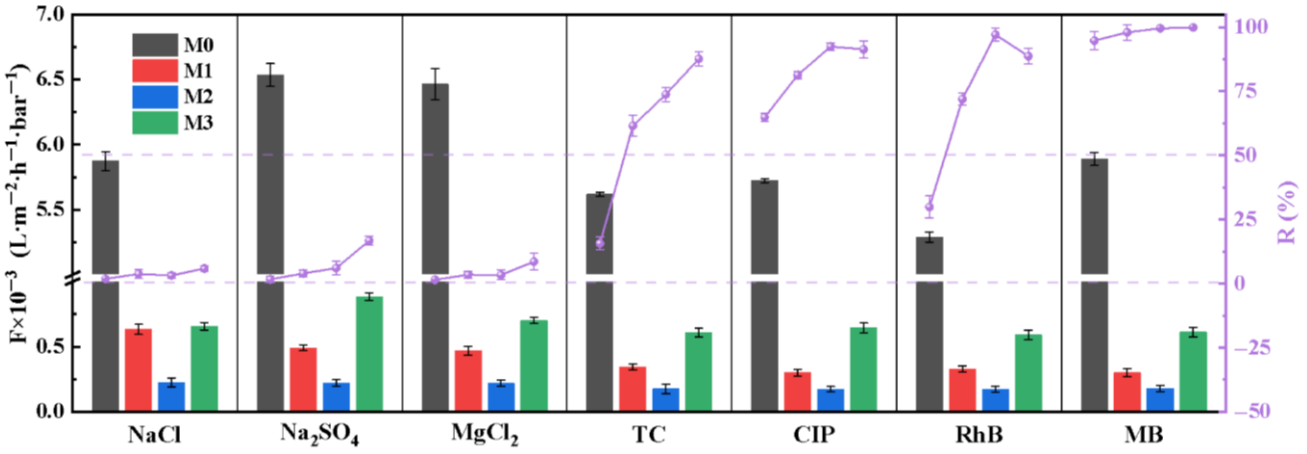


Figure 7. Separation performance of the membranes including rejection and permeate flux.

3.3. Self-Cleaning Performance of the BiOCl@GO/PI Membrane

Two-dimensional membrane materials with layered nanoscale channels are commonly used for screening dyes and micropollutants [34]. However, separated contaminants could accumulate and clog the membrane surface or pores, leading to membrane fouling and subsequent deterioration in performance [35]. Incorporating photocatalytic materials into the membrane separation layer structure enables the effective removal of accumulated contaminants without the need for chemical cleaning. As shown in Figure 8a, in the dark condition, the rejection of M3 to dye decreased from 83.1 to 53.5% after five cycles, while its flux decreased by 17.7% due to membrane fouling from the adsorption of dye. Yet, under UV irradiation, the rejection of M3 to dye remains essentially unchanged, while its flux decreased by only 8.1%. These experimental results confirm that the composite membrane M3 possesses an excellent self-cleaning capability when exposed to UV light, effectively degrading the organic compounds that adhere to its surface arising from the introduction of photocatalytic BiOCl nanocrystals [36].

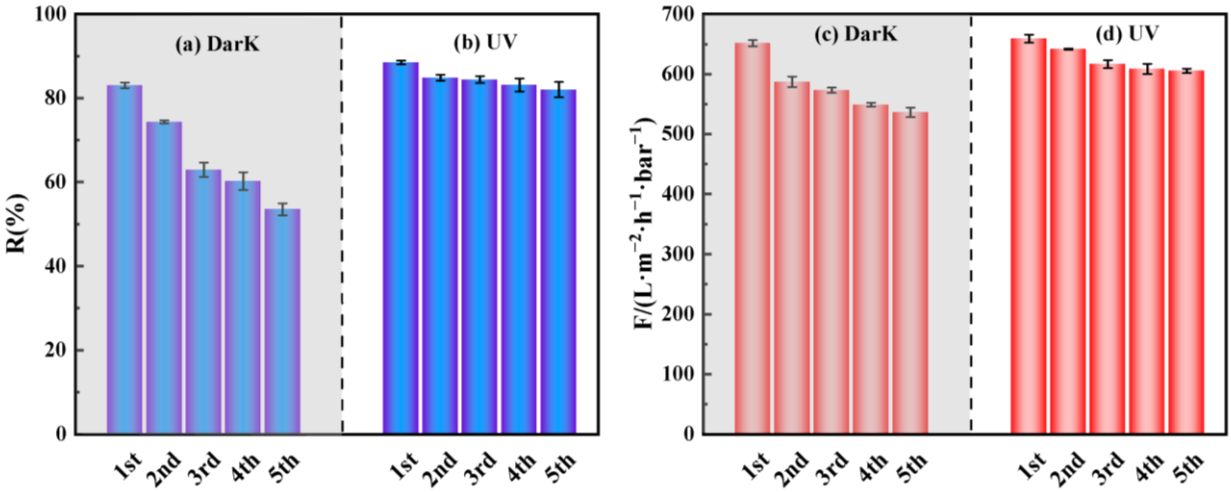


Figure 8. Study on self-cleaning performance of composite membrane M3 during five cycles (200 mL of 20 mg L^{-1} RhB solution). (**a**) Rejection declines under dark condition; (**b**) rejection declines under UV condition; (**c**) flux declines under dark condition; (**d**) flux declines under UV condition.

To investigate the reasons behind the membrane's highly efficient self-cleaning properties, we have examined its photocatalytic activity. Figure 9 shows the degradation performance of M3 when treating 100 mL of different organics at an initial concentration of

10 mg L^{-1}. In Figure 9a, under dark conditions, the RhB concentration remains virtually unchanged. After the addition of M3, the RhB concentration is decreased by around 22% due to the adsorption. Under UV irradiation, the M3 degrades 97.6% of RhB, whereas the dye concentration decreased by only 18% in the absence of a membrane within the same time frame of 2.5 h. Figure 9b shows the photocatalytic performance of M3 in degrading MB. Compared to the dark condition, the M3 degrades 96.0% of MB within 3.5 h. The M3 also exhibits an excellent photocatalytic degradation activity against the antibiotics TC and CIP, as shown in Figure 9c,d. It degrades 97.5% of TC and 98.2% of CIP within 4.5 h. The introduction of nanophotocatalysts endows M3 with excellent photocatalytic degradation activity towards various organic compounds. Consequently, under UV irradiation, the membrane can degrade pollutants deposited on its surface into smaller molecules, thereby mitigating membrane fouling and achieving a superior self-cleaning performance.

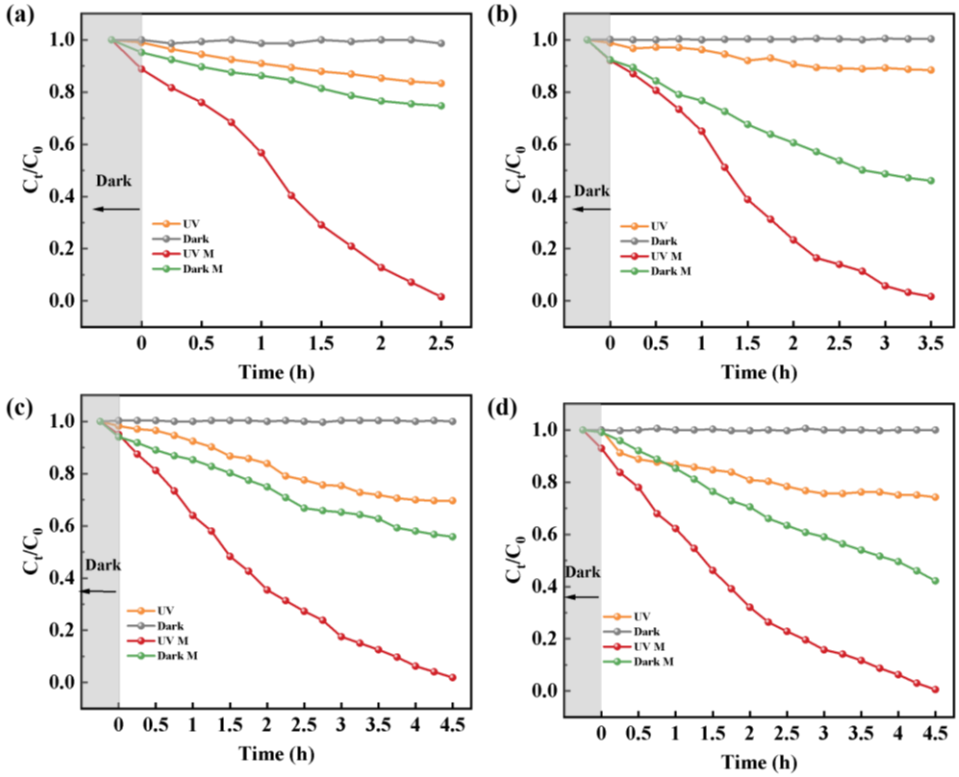


Figure 9. Photodegradation performance of composite membrane M3 against (**a**) RhB, (**b**) MB, (**c**) TC, and (**d**) CIP.

To investigate the role of reactive species in the photocatalytic degradation of TC by the composite membrane M3, various radical scavengers were added into the reaction system and experiments were conducted to detect reactive species. IPA, PBQ, and EDTA-2Na were selected as scavengers for hydroxyl radicals (·OH), superoxide radicals ($\cdot O_2^-$), and holes (h^+), respectively. Figure 10 shows the extent to which photocatalytic activity is inhibited by the different scavengers. The addition of IPA reduces the photocatalytic degradation efficiency of TC by 23.0%, indicating that ·OH plays a role in TC photocatalytic degradation. The TC photocatalytic degradation efficiency decreased by 13.2% because of the addition of EDTA-2Na, suggesting that holes (h^+) are generated during the degradation process. In the photocatalytic system, with the addition of PBQ, the TC photocatalytic degradation rate decreased to 46.7%, suggesting that $\cdot O_2^-$ is the key active species in TC degradation. These results suggest that ·OH, $\cdot O_2^-$, and h^+ are all active species, with $\cdot O_2^-$ being the most active in the photocatalytic degradation of TC. The proposed self-cleaning

mechanism is illustrated in Figure 10b. When the membrane is exposed to UV irradiation, electrons and holes within the material are separated. Electrons (e^-) are excited from the valence band (VB) into the conduction band (CB), leaving positively charged holes (h^+). These charge carriers react with surrounding water and oxygen to produce reactive oxygen species (ROS) such as $\cdot O^{2-}$, which efficiently degrade the organic pollutants on the surface of membrane into CO_2 and H_2O, thereby maintaining the membrane's high self-cleaning performance. In contrast, membranes not exposed to UV radiation exhibit significant performance degradation within five cycles; see Figure 8a.

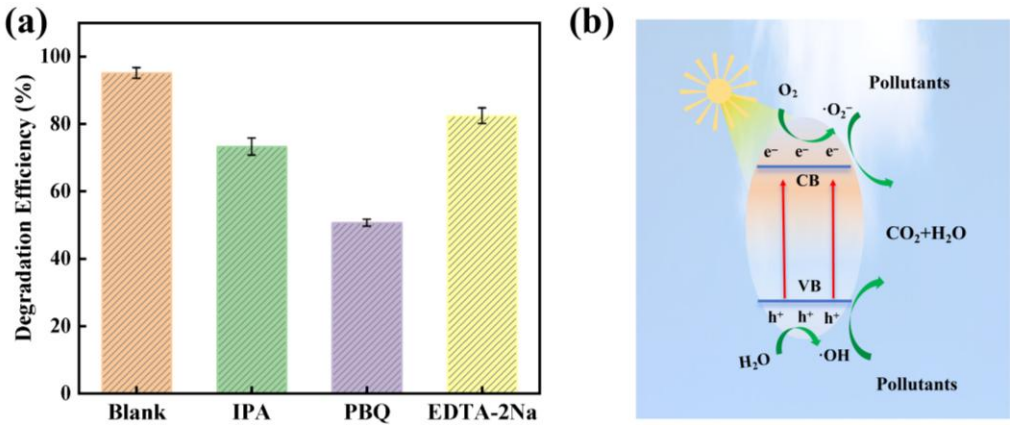


Figure 10. (**a**) Photodegradation efficiency of M3 with different radical trapping agents and (**b**) proposed mechanism of self-cleaning performance.

To investigate the stability and reusability of the photocatalytic membrane M3, its photocatalytic performance was tested for five cycles and 80 h. As shown in Figure 11, the TC degradation efficiency by M3 membrane decreased from 97.5 to 88.3%. The photocatalytic activity of the membrane is still high after five cycles, demonstrating its excellent stability. This is attributed to the mussel-inspired PDA firmly anchoring the nanocatalysts between GO layers.

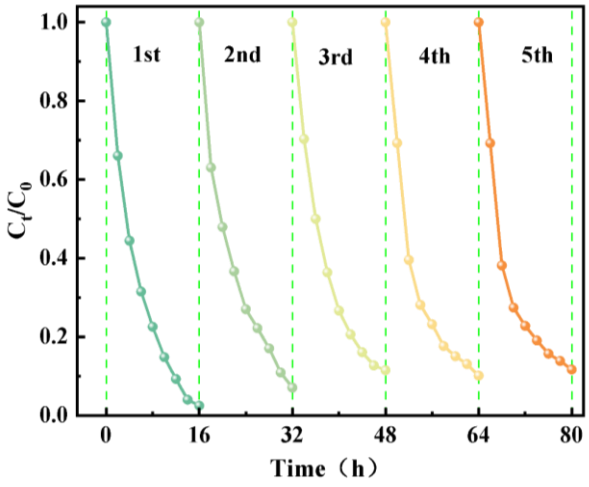


Figure 11. Cycle stability of the composite membrane M3.

4. Conclusions

In this study, a series of BiOCl@GO/PI composite membranes were produced using the vacuum filtration method, which involves intercalating BiOCl nanoparticles between graphene oxide (GO) layers. The presence of BiOCl nanoparticles significantly improves

the hydrophilicity of the composite membranes, achieving a water contact angle of 11.9°. The composite membranes exhibit a high rejection of antibiotics such as TC (87.6%) and CIP (92.4%), and dyes including RhB (97.1%) and MB (99.8%). However, they exhibit low rejection of different salts, making them excellent candidates for the desalination of antibiotics and dyes. Notably, the composite membranes exhibit an outstanding self-cleaning performance and maintain an excellent separation performance under UV irradiation. While the flux gradually decreases to 91.9% of the initial value after UV irradiation, the dye removal rate of the composite membrane remains essentially unchanged. This high self-cleaning performance originates from the BiOCl nanocrystals between the GO layers, which have a high photocatalytic degradation efficiency. Integrating membrane separation technology with photocatalytic technology enhances the photocatalytic activity of the composite membranes, providing new approaches and insights for the comprehensive utilization of water resources.

Author Contributions: Methodology, validation, formal analysis, data curation, and writing—original draft preparation, F.F.; investigation, formal analysis, data curation, Z.Z., J.L., Y.K. and C.Y.; conceptualization, resources, supervision, funding acquisition, writing—review and editing, R.H. and H.G. All authors have read and agreed to the published version of the manuscript.

Funding: This research was funded by National Natural Science Foundation of China (No, 22366021, 22568025), Jiangxi Province Double Thousand Talents Plan (No, jxsq2020101049), China Postdoctoral Science Foundation (No, 2021M691964), Ji'an Natural Science Foundation (No, 20255-061493).

Data Availability Statement: All the data are available at the request of the authors.

Acknowledgments: The authors thank Shiyanjia (https://www.shiyanjia.com/) for the XPS analysis.

Conflicts of Interest: The authors declare no conflicts of interest.

References

1. Wang, C.; Sun, H.; Wang, N.; An, Q.-F. Robust ZIF-8 and Its Derivative Composite Membrane for Antibiotic Desalination with High Performance. *Sep. Purif. Technol.* **2023**, *307*, 122857. [CrossRef]
2. Yang, Z.; Lin, Q.; Zeng, G.; Zhao, S.; Yan, G.; Ang, M.B.M.Y.; Chiao, Y.-H.; Pu, S. Ternary Hetero-Structured BiOBr/Bi2MoO6@MXene Composite Membrane: Construction and Enhanced Removal of Antibiotics and Dyes from Water. *J. Membr. Sci.* **2023**, *669*, 121329. [CrossRef]
3. Basu, S.; Balakrishnan, M. Polyamide Thin Film Composite Membranes Containing ZIF-8 for the Separation of Pharmaceutical Compounds from Aqueous Streams. *Sep. Purif. Technol.* **2017**, *179*, 118–125. [CrossRef]
4. Li, Y.; Han, M.; Chen, J.; Tan, X.; Xie, W.; Lou, H.; Chen, Z.; Gu, H. In-Situ Grown Magnetic Nanoparticles on Graphene Oxide for Removal of Hexavalent Chromium from Wastewater. *Colloids Surf. A Physicochem. Eng. Asp.* **2025**, *712*, 136430. [CrossRef]
5. Li, Y.; Chen, J.; Tan, X.; Lou, H.; Gu, H. Aniline-p-Phenylenediamine Copolymer for Removal of Hexavalent Chromium from Wastewater. *Separations* **2024**, *11*, 327. [CrossRef]
6. Feng, F.; Dong, G.; Wang, J.; Zhu, Z.; Liu, X.; Han, R. Bioinspired PDA/PVDF Composite Membrane with Excellent Antibiotic Desalination Properties. *Emerg. Mater. Res.* **2025**, *14*, 381–388. [CrossRef]
7. Zeng, J.; Xie, W.; Guo, Y.; Zhao, T.; Zhou, H.; Wang, Q.; Li, H.; Guo, Z.; Xu, B.B.; Gu, H. Magnetic Field Facilitated Electrocatalytic Degradation of Tetracycline in Wastewater by Magnetic Porous Carbonized Phthalonitrile Resin. *Appl. Catal. B Environ.* **2024**, *340*, 123225. [CrossRef]
8. Zhu, Z.; Feng, F.; Li, J.; Wang, G.; Dong, G.; Han, R. Selective Solvent Resistant Polyimide Composite Membranes with Efficient Separation Performance in Antibiotics. *Results Eng.* **2025**, *29*, 108653. [CrossRef]
9. Lim, S.K.; Goh, K.; Bae, T.-H.; Wang, R. Polymer-Based Membranes for Solvent-Resistant Nanofiltration: A Review. *Chin. J. Chem. Eng.* **2017**, *25*, 1653–1675. [CrossRef]
10. Dong, G.; Feng, F.; Su, S.; Zhu, Z.; Liu, X.; Han, R. Facile Preparation of Quaternary Ammonium Graft-Modified PVDF Nanofiltration Membrane with Excellent Antibiotic Desalination and Antibacterial Performance. *J. Water Process Eng.* **2026**, *81*, 109284. [CrossRef]

11. Cheng, K.; Zhang, N.; Yang, N.; Hou, S.; Ma, J.; Zhang, L.; Sun, Y.; Jiang, B. Rapid and Robust Modification of PVDF Ultrafiltration Membranes with Enhanced Permselectivity, Antifouling and Antibacterial Performance. *Sep. Purif. Technol.* **2021**, *262*, 118316. [CrossRef]
12. Han, R.; Feng, F.; Zhu, Z.; Dong, G.; Liu, X.; Guo, M.; Yang, X.; Qin, J.; Wang, H.; Dai, Y.; et al. Engineering Multifunctional MDPCs@MOFs via Selective Thermal Etching Integrates Low-Resistance Transport with Strong Adsorption for Enhanced CO_2/N_2 Separation. *J. Colloid Interface Sci.* **2025**, *708*, 139760. [CrossRef]
13. Khan, A.; Li, W.; Ma, X.; Dong, M.; Geng, L.; Khan, S.S.; Li, Y.; Khan, S.; Yasin, G. Large-Scale with Uniformly Dispersed Silver Nanoparticles Decorated Poly(Acrylonitrile) (PAN) Membrane Preparation for Efficient Photocatalytic Reactions and Antimicrobial Activity. *Opt. Mater.* **2024**, *149*, 115063. [CrossRef]
14. Yu, S.; Wang, Y.; Sun, F.; Wang, R.; Zhou, Y. Novel Mpg-C_3N_4/TiO_2 Nanocomposite Photocatalytic Membrane Reactor for Sulfamethoxazole Photodegradation. *Chem. Eng. J.* **2018**, *337*, 183–192. [CrossRef]
15. Zhang, Q.; Wang, H.; Fan, X.; Lv, F.; Chen, S.; Quan, X. Fabrication of TiO_2 Nanofiber Membranes by a Simple Dip-Coating Technique for Water Treatment. *Surf. Coat. Technol.* **2016**, *298*, 45–52. [CrossRef]
16. Chen, C.; Fei, L.; Wang, B.; Xu, J.; Li, B.; Shen, L.; Lin, H. MOF-Based Photocatalytic Membrane for Water Purification: A Review. *Small* **2024**, *20*, 2305066. [CrossRef]
17. Sasikala, V.; Karthik, P.; Ravichandran, S.; Prakash, N.; Rajesh, J.; Mukkannan, A. Facile Synthesis of BiOCl Incorporated Polymer Membrane for Effective Photocatalytic Dye Degradation. *J. Polym. Environ.* **2024**, *32*, 1937–1951. [CrossRef]
18. Duan, H.; Zhuang, Z.; Yang, J.; Zhang, S.; Wang, L. Confined Gas Transport in Low-Dimensional Materials. *Int. J. Smart Nano Mater.* **2024**, *15*, 127–164. [CrossRef]
19. Salemi, F.; Karimzadeh, F.; Abbasi, M.-H.; Moradi, F.; Pham, D.H.; Kim, J. Effective Parameters on Polydimethylsiloxane/Graphene Composite-Based Triboelectric Nanogenerator Performance. *Int. J. Smart Nano Mater.* **2024**, *15*, 365–386. [CrossRef]
20. Ruiz-Torres, C.A.; Kang, J.; Kang, S.; Kim, J.P.; Kim, C.; Kang, K.M.; Cho, K.M.; Nam, Y.T.; Chang, Y.-Y.; Byon, C.; et al. Oxidation-Controlled Nanoporous Graphene Laminate Membranes via Intercalation Chemistry for Desalination. *J. Membr. Sci.* **2025**, *735*, 124515. [CrossRef]
21. Ma, L.; Shi, X.; Zhang, G.; Wen, X.; Liu, C.; Ma, X.; Jiang, M.; Li, J.; Zhang, L. A Stable Bimetallic MOF (Ti, Zr)-Graphene Oxide Composite Membrane with Synergistic Anti-Fouling Strategy of Photocatalysis and Hydration Layer for Efficient Separation of Oily Emulsions. *Sep. Purif. Technol.* **2026**, *382*, 136016. [CrossRef]
22. Joseph, A.; Yelekar, G.R.; Vijayanandan, A. Efficiency of Titanium Dioxide-Reduced Graphene Oxide in Carbamazepine Removal: A Comparative Study of Adsorption, Photocatalysis, and Ultrafiltration Techniques. *Appl. Catal. O Open* **2024**, *193*, 206967. [CrossRef]
23. Runlin, H.; Chaoyue, W.; Congcong, B.; Hanli, W. Facile Preparation of High Performance GO/Mn_3O_4/PVDF Composite Membranes with Intercalation of Manganese Oxide Nanowires. *RSC Adv.* **2023**, *13*, 19002–19010. [CrossRef] [PubMed]
24. Chen, L.; Shi, G.; Shen, J.; Peng, B.; Zhang, B.; Wang, Y.; Bian, F.; Wang, J.; Li, D.; Qian, Z.; et al. Ion Sieving in Graphene Oxide Membranes via Cationic Control of Interlayer Spacing. *Nature* **2017**, *550*, 415–418. [CrossRef] [PubMed]
25. Wang, H.; Zhang, L.; Chen, R.; Liu, Q.; Liu, J.; Yu, J.; Liu, P.; Duan, J.; Wang, J. Surface Morphology Properties and Antifouling Activity of Bi_2WO_6/Boron-Grafted Polyurethane Composite Coatings Realized via Multiple Synergy. *J. Colloid Interface Sci.* **2022**, *626*, 815–823. [CrossRef]
26. Feng, F.; Zhu, Z.; Li, J.; Su, S.; Dong, G.; Wang, G.; Liu, X.; Han, R. In-Situ Grown Electrospun PI/BiOCl Nanofiber Membranes for Efficient Photocatalytic Degradation of Antibiotics. *J. Photochem. Photobiol. A Chem.* **2026**, *474*, 117014. [CrossRef]
27. Liao, H.; Liu, C.; Zhong, J.; Li, J. Fabrication of BiOCl with Adjustable Oxygen Vacancies and Greatly Elevated Photocatalytic Activity by Using Bamboo Fiber Surface Embellishment. *Colloids Surf. A Physicochem. Eng. Asp.* **2022**, *634*, 127892. [CrossRef]
28. Le, T.M.H.; Chuchak, R.; Sairiam, S. Empowering TiO_2–Coated PVDF Membranes Stability with Polyaniline and Polydopamine for Synergistic Separation and Photocatalytic Enhancement in Dye Wastewater Purification. *Sci. Rep.* **2024**, *14*, 15969. [CrossRef]
29. Han, R.; Wu, K.; Xu, L. Facile Preparation of Loose P84 Copolyimide/GO Composite Membrane with Excellent Selectivity and Solvent Resistance. *Polymers* **2022**, *14*, 1353. [CrossRef] [PubMed]
30. Cheng, X.; Liao, J.; Xue, Y.; Lin, Q.; Yang, Z.; Yan, G.; Zeng, G.; Sengupta, A. Ultrahigh-Flux and Self-Cleaning Composite Membrane Based on BiOCl-PPy Modified MXene Nanosheets for Contaminants Removal from Wastewater. *J. Membr. Sci.* **2022**, *644*, 120188. [CrossRef]
31. Han, R.; Feng, F.; Zhu, Z.; Su, S.; Wang, J.; Shi, C.; Dong, G.; Gu, H. Innovative Bi-Functional Cellulose Acetate/BiOCl Photocatalytic Membrane with Excellent Antibiotics Degradation and Photoresponsive Antimicrobial Performance. *Colloids Surf. A Physicochem. Eng. Asp.* **2026**, *730*, 138959. [CrossRef]
32. Kral, M.; Dendisova, M.; Svoboda, J.; Cernescu, A.; Svecova, M.; Johnson, C.M.; Pop-Georgievski, O.; Matejka, P. Nano-FTIR Spectroscopy of Surface Confluent Polydopamine Films—What Is the Role of Deposition Time and Substrate Material? *Colloids Surf. B Biointerfaces* **2024**, *235*, 113769. [CrossRef]

33. Liu, H.; Yang, C.; Huang, J.; Chen, J.; Zhong, J.; Li, J. Ionic Liquid-Assisted Hydrothermal Preparation of BiOI/BiOCl Heterojunctions with Enhanced Separation Efficiency of Photo-Generated Charge Pairs and Photocatalytic Performance. *Inorg. Chem. Commun.* **2020**, *113*, 107806. [CrossRef]
34. Petukhov, D.I.; Weston, J.; Valeev, R.G.; Johnson, D.J. Graphene Oxide Surface Modification of Reverse Osmosis (RO) Membrane via Langmuir–Blodgett Technique: Balancing Performance and Antifouling Properties. *Membranes* **2024**, *14*, 172. [CrossRef] [PubMed]
35. Petukhov, D.I.; Chumakov, A.P.; Johnson, D.J. Effect of Competition between Swelling and Dye Adsorption on the Performance and Selectivity of Graphene Oxide Membranes. *Nanoscale* **2025**, *17*, 25572–25588. [CrossRef] [PubMed]
36. Song, P.; Du, J.; Shi, Y.; Fang, X.; Ma, X.; Liu, D.; Cao, D.; Li, J.; Chen, R.; Wu, C.; et al. Highly Active 3D Composites for a Flow-Through Photocatalytic Membrane Reactor toward Water Micropollutant Removal. *ACS Mater. Lett.* **2024**, *6*, 427–437. [CrossRef]

Disclaimer/Publisher's Note: The statements, opinions and data contained in all publications are solely those of the individual author(s) and contributor(s) and not of MDPI and/or the editor(s). MDPI and/or the editor(s) disclaim responsibility for any injury to people or property resulting from any ideas, methods, instructions or products referred to in the content.